In-Vitro Study of Speed and Alignment Angle in Cochlear Implant Electrode Array Insertions

Philipp Aebischer, Georgios Mantokoudis, Stefan Weder, Lukas Anschuetz, Marco Caversaccio, and Wilhelm Wimmer

Abstract*—*Objective: **The insertion of the electrode array is a critical step in cochlear implantation. Herein we comprehensively investigate the impact of the alignment angle and feed-forward speed on deep insertions in artificial scala tympani models with accurate macro-anatomy and controlled frictional properties.** ***Methods:*** **Motorized insertions (n=1033) were performed in six scala tympani models with varying speeds and alignment angles. We evaluated reaction forces and micrographs of the insertion process and developed a mathematical model to estimate the normal force distribution along the electrode arrays.** ***Results:*** **Insertions parallel to the cochlear base significantly reduce insertion energies and lead to smoother array movement. Non-constant insertion speeds allow to reduce insertion forces for a fixed total insertion time compared to a constant feed rate.** ***Conclusion:*** **In cochlear implantation, smoothness and peak forces can be reduced with alignment angles parallel to the scala tympani centerline and with non-constant feed-forward speed profiles.** ***Significance:*** **Our results may help to provide clinical guidelines and improve surgical tools for manual and automated cochlear implantation.**

***Index Terms*—Free fitting array, lateral wall array, robotic cochlear implantation, insertion trajectory, friction force model, cochlear shape.**

I. Introduction

ATRAUMATIC insertion of the electrode array into the scala tympani is not always achieved in cochlear implantation. Documented injuries include the penetration of the spiral ligament, osseous spiral lamina fractures, the elevation or rupture of the basilar membrane and array translocation into the scala media and scala vestibuli [1]–[4]. Direct trauma can cause inflammatory response, apoptosis and fibrosis development [5], affecting both electrical and acoustic hearing and limiting qualification for future therapeutic approaches [6], [7].

Since the initial work in 1993 defining the soft surgery protocol by Lehnhardt [8], numerous studies have explored strategies to minimize insertion trauma [7], [9]–[11]. The adaption of a slow electrode insertion speed was shown to promote the preservation of residual hearing [12]. Due to the limited force perception threshold and minimum speed of continuous hand movements in manually performed insertions [13]–[16], automated insertion tools [17]–[21] and force measuring arrays [22], [23] have been proposed. A correlation between non-optimal insertion axes, insertion forces and intracochlear trauma was observed in ex-vivo experiments [24], [25]. To reduce insertion forces, modern electrode array designs tend toward smaller diameters and lower bending stiffness [5], [26]–[28].

Several studies addressed the insertion of electrode arrays into cadaveric temporal bone specimens [2], [24], [29]–[34] and artificial cochlea models [15], [19], [35], [36]. The main advantage of cadaver specimens is the presence of intracochlear structures that enable monitoring of damage by the electrode array. On the downside, cadaveric samples vary in their anatomy and can only be used for a limited number of insertions. They allow no direct observation of the electrode array movement and the specimen preservation affects the characteristics of the biological tissue [34]. Therefore, artificial models can be a valid option for initial testing and experimental validations.

The aim of this study was to improve our understanding of the mechanics of the insertion of lateral wall cochlear implant (CI) electrode arrays. Such an analysis is essential for designing surgical instruments and could be used to refine current clinical guidelines. Using physical models, we investigated the influence of the alignment angle, feed-forward speed profile, and cochlear shape on the occurring insertion forces and array movement.

II. Materials and Methods

A. Experimental Setup

In the experiments, we inserted dummies of lateral wall CI electrode arrays into artificial scala tympani models based on micro-computed tomography images of human subjects [37], [38]. Our models reproduce the 3D anatomy and have properties consistent with cadaveric specimens regarding the force

Manuscript received February 15, 2021; revised May 6, 2021 and June 7, 2021; accepted June 7, 2021. Date of publication June 10, 2021; date of current version December 23, 2021. This work was supported in part by Eurostars E! 11597 RCI research grant, the J&K Wonderland foundation, the Georges und Jenny Bloch foundation, and the CID & CD Charity Foundation. *(Corresponding author: Philipp Aebischer.)*

Philipp Aebischer is with the Department for Otolaryngology, Head and Neck Surgery, Inselspital University Hospital Bern, 3010 Bern, Switzerland, and also with the Hearing Research Laboratory, ARTORG Center for Biomedical Engineering Research, University of Bern, 3012 Bern, Switzerland (e-mail: philipp.aebischer@artorg.unibe.ch).

Georgios Mantokoudis, Stefan Weder, and Lukas Anschuetz are with the Department for Otolaryngology, Head and Neck Surgery, Inselspital University Hospital Bern, Switzerland.

Marco Caversaccio and Wilhelm Wimmer are with the Department for Otolaryngology, Head and Neck Surgery, Inselspital University Hospital Bern, Switzerland and also with the Hearing Research Laboratory, ARTORG Center for Biomedical Engineering Research, University of Bern, Switzerland.

This article has supplementary downloadable material available at https://doi.org/10.1109/TBME.2021.3088232, provided by the authors.

Digital Object Identifier 10.1109/TBME.2021.3088232

TABLE I
GEOMETRIC INFORMATION OF THE SIX COCHLEAE AND BREAKDOWN OF THE INSERTION EXPERIMENTS PER MODEL

source	label	length	width	height	wall length	volume	exploratory	mediolateral sweep	two axis sweep	speed sweep	non-constant speeds
Sicas AS1-80591	A	8.6	6.9	3.8	31	26	4 (1)	33 (5)			
Sicas AS1-80593	B	9.2	6.9	3.7	32	28	394 (15)	63 (6)	85 (5)	55 (5)	117 (10)
OpenEar Zeta	C	9.0	7.0	3.8	32	33		29 (4)			
OpenEar Gamma	D	8.7	7.4	3.7	34	39	68 (4)	32 (4)	34 (2)		
Sicas DS1-29503	E	9.3	7.4	3.9	36	41	1 (1)	48 (4)	51 (2)		
OpenEar Eta	F	10.0	7.4	3.8	36	47		23 (3)			
		dimensions in mm or mm^3					number of insertions (number of dummies used)				

length: Distance in the basal plane from the round window through the center of the modiolus to the opposite lateral wall, also referred to as A-value [34].
width: Distance in the basal plane orthogonal to the length, along the short axis of the cochlea, also referred to as B-value [42].
height: Distance from the center of the modiolus in the basal plane to the apex of the cochlea.
wall length: Distance along the lateral wall of the first two cochlear turns starting at the round window.
volume: Volume of the scala tympani cropped after two cochlear turns.

progression during insertion and the speed dependence of insertion forces [39].

Six models made from clear epoxy resin with different geometries were produced. An overview of their geometry parameters are provided in Table I. The scala tympani models are designated by letters from *A* to *F* corresponding to the length of the lateral wall in ascending order.

To enable a large number of insertions, we produced electrode array dummies that match the mechanical characteristics of a long free-fitting clinical array (Flex^{28}, MED-EL GmbH, Innsbruck, Austria) [39]. We chose this particular type of array because it is the most commonly used in our clinic and enables us to monitor deep insertions [40], [41]. The dummies have the same dimensions as the clinical arrays, with a circular cross-section (diameter 0.8 mm) at the base morphing into an elliptical shape (0.5 mm $\times$ 0.4 mm) at the tip. Both dummies and scala tympani models were coated with a polymer brush coating that provides a hydrophilic surface mimicking the contact with the periosteum and the spiral ligament which covers the lateral wall of the scala tympani. The detailed methods for the fabrication of the electrode array dummies and the synthetic models are presented in [39].

The measurements were performed on a bench-top setup for motorized CI electrode array insertions that records the insertion force, photo-micrographs and intracochlear pressure (c. f., Fig. 1). A bowden cable connected to a linear actuator (LGA20, Nanotec Electronic GmbH & Co. KG, Feldkirchen, Germany) was used to push the dummies out of a guide tube into a scala tympani model mounted to a unidirectional load cell. At the apex, the models have a 1 mm wide duct co-linear to the modiolar axis, at the end of which a micro-electromechanical pressure sensor was attached.

The setup was designed to allow adjusting the alignment angle of the insertion tube while keeping the scala tympani model in a fixed position to avoid gravitational effects. To that end, the load cell was mounted to a rotating platform, so that the direction of the force measurement matched the axis of the insertion.

The scala tympani orientation in a typical surgical setting was evaluated from photographs of a cochlear implantation at our

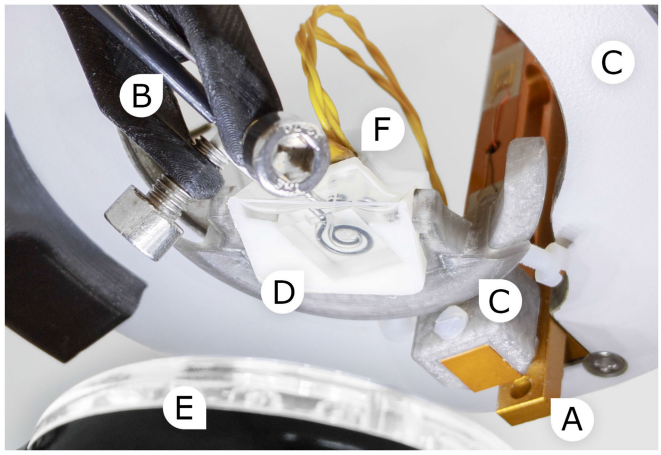

Fig. 1. The load cell (A) and insertion guide tube (B) are mounted on opposite sides of a circular base plate (C). Insertion angles can be adjusted by rotating the base plate about two axes around the scala tympani model (D), which remains in a fixed orientation. A microscope records the insertion perpendicular to the basal plane and a LED ring (E) ensures uniform illumination. A pressure sensor (F) connects to the apex of the scala tympani model. The dummy arrays are pushed forward with a bowden cable leading to a linear actuator (not depicted). Control of the actuator and recording of sensor data is performed on a Raspberry Pi.

institution. In accordance with the standard clinical protocol, the patient was bedded in a lateral position with the head in hyperextension. The rotation that transforms the local cochlear coordinate system (according to Verbist *et al.* [43], [44], c. f., Fig. 2) to this orientation can be expressed by the Euler angles $(\alpha = 90°, \beta = 52°, \gamma = -65°)$.

B. Data Acquisition

The setup records the intracochlear pressure (MS5837-02BA, Measurement Specialties, Inc., Hampton, USA), the reaction force in the direction of the insertion (KD78, ME Meßsysteme GmbH, Hennigsdorf, Germany and HX711 load cell amplifier, SparkFun Electronics, Niwot, USA) and photo-micrographs

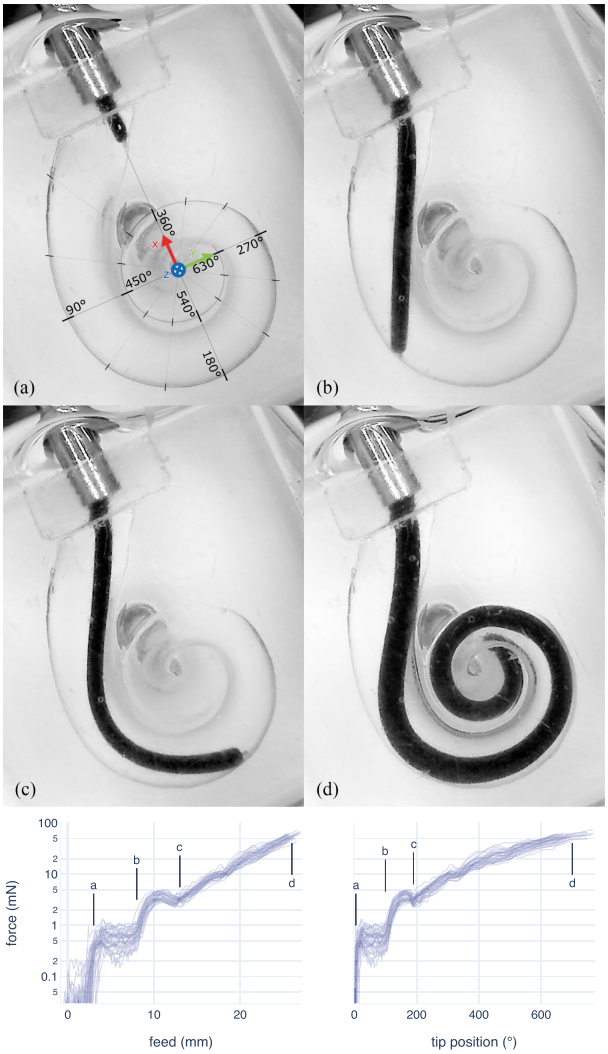

Fig. 2. Top: Images for a moderately angled insertion (20° mediolateral, 20° basoapical). (a) First contact with modiolar wall, (b) contact with lateral wall, (c) Array bows outwards to the lateral wall, (d) Full insertion. Bottom: Insertion forces as a function of the linear feed and angular insertion depth, respectively. The graph shows 39 repetitions with 7 dummies inserted at 0.33 mm/s into model *B*. For reference, the angular insertion depth is indicated on the first image.

co-planar to the basal turn (USB Digital Microscope, Z-Star Microelectronics Corporation).

The load cell has a rated accuracy of 0.1 mN and records 86 samples/s at a measured noise floor of $F_{\mathrm{RMS}} = 0.04$ mN. The pressure sensor has a rated accuracy of 50 Pa and records 23 samples /s at a noise floor of $P_{\mathrm{RMS}} = 2$ Pa. The microscope captures images at a resolution of $640\ \mathrm{P} \times 480\ \mathrm{P}$ at a rate of 20 images/s.

C. Data Processing and Outcome Measures

1) Automatic Centerline Detection: Post-processing was performed in Python using the SciPy software package and OpenCV library. The electrode array centerlines were computed by subtracting a pre-insertion reference image of the model from the images taken during the insertion. The differential image was thresholded and the largest connected component selected as the electrode array contour. The contour was cleaned by subsequent application of a closing and erosion filter and the centerline determined by applying a Guo-Hall thinning algorithm and fitting a cubic spline into the resulting points.

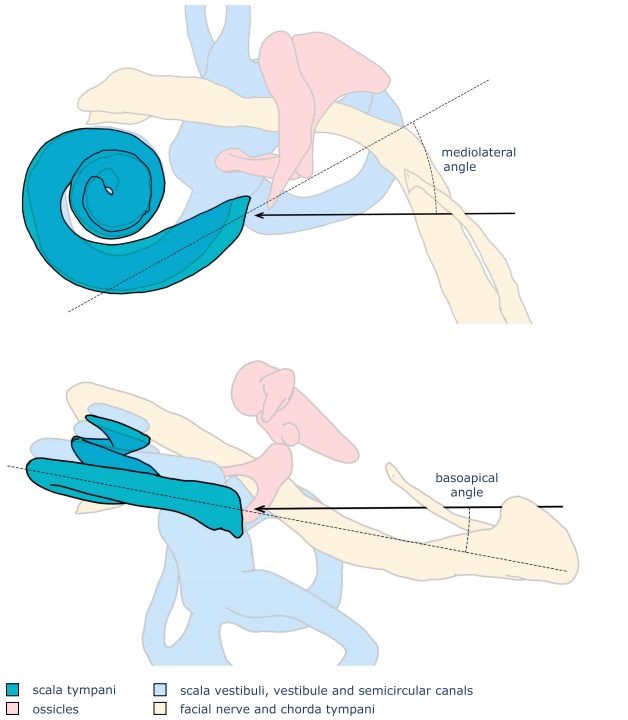

Fig. 3. The axis along which an electrode array is inserted (black arrow) can be described with two angles. Top: The projection into the basal plane defines the mediolateral angle (also referred to as in-plane angle [45]). The zero-degree reference is defined by the axis that passes through the round window and is tangential to the scala tympani centerline. Positive values direct the electrode tip towards the modiolus. Bottom: The angle between the basal plane and the insertion axis defines the basoapical angle (also referred to as out-of-plane angle [45]). Positive values direct the electrode tip towards the posterior margin of the scala tympani.

2) Angular Coordinates: The angular insertion depth was defined as the azimuth coordinate of the end-point of the electrode array centerline in the local cylindrical coordinate system. A grid showing these angular coordinates is overlaid on the first image of Fig. 2.

3) Insertion Axis: For visualization purposes, the insertion axis was separated into the component in the basal plane (denoted mediolateral angle) and the component orthogonal to this plane (denoted basoapical angle) [45]. A mediolateral angle of zero degrees is defined by the line that passes through the round window and is tangent to the scala tympani centerline. A parallel insertion refers to one in which both the mediolateral and basoapical angles are 0°. An illustration of these angles is shown in Fig. 3.

4) Clinical Insertion Axes: To study realistic insertion axes, anatomically accessible insertion angles were estimated by analyzing CT images of 39 subjects implanted at our institution with the same lateral wall electrode array through the round window [40]. An estimation of the minimally accessible angle to the scala tympani can be obtained by determining the tangent at which the electrode array enters the scala tympani, because the flexible arrays inherently minimize curvature. The details of the analysis are provided as a supplementary material. We measured

angles of $18^\circ \pm 13^\circ$ (mean and standard deviation) mediolateral and $10^\circ \pm 11^\circ$ basoapical.

5) Insertion Work: To compare the insertions at different feed rates while also including the force progression during the insertion, the forces were integrated over the feed forward position to yield the work required for the array insertion.

6) Array Tip Speed: The speed of the array tip was computed from the endpoint coordinate of the automatically segmented electrode array centerline. Since in our setup, an insertion speed of 0.33 mm/s translates to roughly 1 P/frame, the tip coordinates were first smoothed with a moving average filter (window width 40 frames). Then the speed is obtained by dividing the Euclidean norm of the difference of the coordinates of successive frames by their corresponding time difference.

7) Array Curvature: The curvature of a specific part of a dummy array was defined as the inverse of the radius of a circle fitted into local points on the array. For the curvature in the basal turn, points with an angular depth between 45° and 135° were selected. For the curvature at the round window, points below an angular depth of 22.5° were selected. An additional point on the tip of the guide tube was manually added, since this location is not included in the automatically extracted electrode array centerline.

D. Study Protocol

The study is divided into experiments on the alignment angle, the insertion speed, and the cochlear shape. A constant speed of 0.33 mm/s, a mediolateral angle of 20° and a basoapical angle of 0° were chosen as default values. To investigate a particular parameter, a sweep was performed while all other parameters remained fixed at their default values. The mediolateral angle corresponds to the average minimally accessible angle as evaluated in Section II-C4 ($18^\circ \pm 13^\circ$), and the basoapical angle was chosen because it is within one standard deviation of the clinically observed mean value ($10^\circ \pm 11^\circ$) while minimizing potential influences not captured by the photo-micrographs taken co-planar to the basal turn.

Alignment angle and speed were primarily studied with model *B* (c. f., Table I). The cochlear base length of this model corresponds to an average-sized cochlea (9.2 mm) [42].

When performing a sweep on a given parameter, the individual measurements were taken in a randomized order to avoid systematic errors. Periodic control experiments were performed at the default values). In case of an observable degradation (e. g., changing frictional conditions or breakage of a metal wire) the measurements were excluded from the analysis.

1) Insertion Axis: For the investigation of the influence of the alignment angle, 12 combinations of mediolateral and basoapical angles were assessed (between 0° to 40° and -20° to 20°, respectively) with a constant insertion speed of 0.33 mm/s in randomized order.

Because the insertion metrics showed to be less affected by the basoapical angle, a finer stepped sweep of the mediolateral angle at 9 angles from 0° to 40° was conducted with a fixed basoapical angle of 0°.

2) Insertion Speed: Insertions were conducted at 6 constant speeds spaced evenly on a logarithmic scale (0.05 mm/s to 4 mm/s) at the default axis (20° mediolateral and 0° basoapical) and in randomized order. The speed of accelerated insertions was set to 0.1 mm/s for the first 30 s, then smoothly increased to a value of 1 mm/s for the last 4 s. The speed of decelerated insertions was set to 1 mm/s for the first 1 s, then smoothly decreased to a value of 0.05 mm/s for the final 10 s.

3) Cochlear Shape: To evaluate the influence of the cochlear shape, the same angular range of angles as in Section II-D1 was probed for models *D* and *E*. In addition, mediolateral angles of 0°, 20° and 40° were measured with all six models at a fixed basoapical angle of 0°, again at a constant insertion speed of 0.33 mm/s and in randomized order.

In total, we performed 1058 insertion experiments. Of those, 25 were excluded because of degradation, 475 were inserted for exploratory analysis, 390 the investigation of the angular dependency and 172 for investigating the insertion speed dependency. A breakdown of the number of insertions and the number of dummies used with respect to the experiment and model are provided in Table I.

E. Friction Force Model

Insertion forces are caused by mechanical deformation of the electrode array adapting to the cochlear shape and by friction along the contact surface of the array with the scalar lumen. For lateral wall electrodes, the latter is closely related to the belt friction equation that describes the load force F_b which can be held by the holding force F_a through a belt wrapped θ rad around a bollard with friction μ [46]–[48]:

$$F_b(\theta) = F_a e^{\mu\theta} \tag{1}$$

The same formalism can be applied to the case of pushing an array into a convex curvature. In this case, F_a corresponds to the force with which the tip counteracts the insertion. The force F_b applied at the basal end of the array increases exponentially with the angular contact length. Interestingly, this force is independent of the radius.

Kha and Chen determined the frictional coefficient between an electrode array and the endosteum lining of $\mu = 0.12$ [47]. Hence, (1) gives the angular feed θ^* that leads to a doubling of the frictional forces

$$\theta^* = \frac{ln(2)}{\mu} = 331^\circ. \tag{2}$$

The tip resistance force F_a is induced by the bending stiffness of the array, which causes pressure on the lateral wall. Since the friction is known, this normal force can be estimated:

$$N_{\text{tip}} = \frac{F_a}{\mu}. \tag{3}$$

The array's bending stiffness leads to an increase in contact pressure over the entire length that depends on the cochlear shape and is not accounted for in this model. Moreover, plastic deformation causes a dependence on the array's bending history, drastically increasing model complexity [49]. However, as an approximation we can model the additional friction by an effective friction coefficient $\mu_{\text{eff}} > \mu$. Fitting the relation (1) to experimental data yields the parameters μ_{eff} and F_a, and with (3) an estimation of the tip contact force can be given.

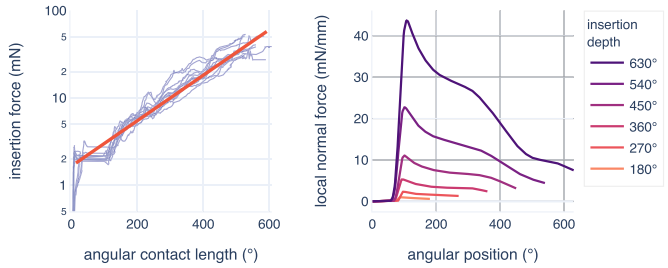

Fig. 4. Left: Insertion forces for parallel insertions increase exponentially with the angular contact length between the electrode array and the lateral wall. The graphs shows 12 experiments with 7 dummies (0° mediolateral and basoapical at 0.33 mm/s, model *B*). The red line indicates the best fit according to (1). Right: Estimation of the line load resulting from the normal force at different angular depths of insertion according to (4).

Following from (1), the normal force $dN(\alpha)$, exerted by a short segment of the array at position α, depends on how far apart this position is from the tip (i. e., $\theta - \alpha$):

$$dN(\alpha) = \mu F_a e^{\mu(\theta-\alpha)} d\alpha. \tag{4}$$

Notably, the normal force is independent of the arrays' contact basally to the considered point. The exponential scaling implies that during the final steps of the insertion, the forces acting on the lateral wall in the basal region of the cochlea are expected to increase substantially.

III. Results

A. Insertion Forces

Fig. 2 summarizes 39 insertions from 7 dummies inserted at 0.33 mm/s and a moderate insertion axis (20° mediolateral, 0° basoapical). Insertion forces scale roughly exponentially with the insertion depth. During the insertion through the basal turn, forces are very low, with small variations caused by the first contact of the dummy array with the modiolus and lateral wall, respectively. Once the array has curved outward and is in contact with the lateral wall, the force progression stabilizes and increases continuously as the contact length increases.

B. Contact Force Distribution

Fitting (1) to the measurements of parallel insertions yielded an effective frictional coefficient of $\mu_{\text{eff}} = 0.34$ and a tip contact force of $N_a = 14$ mN. The data and the best fit are shown in Fig. 4 (12 insertions with 7 dummies, 0° mediolateral, 0° basoapical at 0.33 mm/s). The force increase corresponds to a doubling angle of $\theta^* = 116°$.

From these values, the force acting along scala tympani's lateral wall can be estimated according to (4). This line load is shown in Fig. 4 (right) for different angular insertion depths. For a fully inserted array, 43 mN/mm are observed in the basal region of the scala tympani and 9 mN/mm near the array tip.

C. Insertion Axis

Fig. 5 (bottom) shows the insertion work for different insertion axes in the range of anatomically accessible angles. Forces were lowest for parallel insertions with an average peak force of 35 mN and an average insertion work of 291 μJ. Large alignment angles substantially increase the forces with values of 58 mN and 638 μJ at a mediolateral angle of 40° (0° basoapical, 9 insertions each with 7 dummies, inserted at 0.33 mm/s).

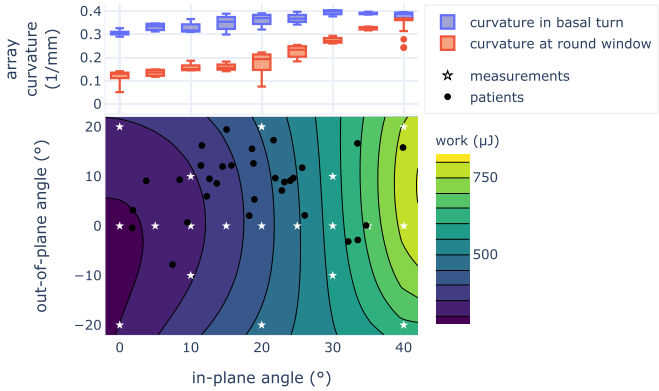

Fig. 5. Bottom: Least squares fit of a bivariate quadratic polynomial to the insertion work as a function of the insertion axis. White stars indicate the measured insertion trajectory alignment angles, black dots indicate the accessible insertion axes estimated from CT images of implanted patients. Top: Curvature of dummies inserted at a basoapical angle of 0° at the round window (red) and in the basal turn (blue). The graph combines a sweep on a uniform grid and a sweep along a basoapical angle of 0°, resulting in 4-9 insertions per axis using 2-5 dummies. All insertions were carried out at 0.33 mm/s into model *B*.

After the insertion, the array relaxes to its final configuration within a few seconds, relieving residual stresses. This decrease in force amounts to 17 mN±4 mN, independent of the insertion axis (average of all 131 insertions in this series of experiments, with mediolateral angles between 0° to 40° and basoapical angles between −20° to 20°, inserted at 0.33 mm/s).

With non-zero mediolateral angles, the array has contact points first medially along the modiolus and then along the lateral wall. The curvature associated with this s-shape is shown in Fig. 5 (top) for the electrode array dummies inserted with a basoapical angle of 0°. The array bends more tightly at the round window region for larger mediolateral angles. The same trend is observed where the array curves back into the basal turn. On the other hand, we observed no statistically significant difference in the shape of the arrays above 150° for different insertion angles (independent two-sample t-test).

D. Cochlear Shape Variations

Fig. 6 compares the insertion forces in six different models as a function of linear and angular insertion depth. The models are sorted by their cochlear size. Larger insertion forces were observed for smaller sized models (Pearson's correlation coefficient $r = -0.84$, $p = 0.03$).

Interestingly, we found that the difference between the forces of parallel and non-parallel insertions yields a model-independent force difference that increases with the feed-forward position (Fig. 6, top right). In contrast, the differences vary more between each other when obtained as a function of angular insertion depth (same figure, bottom right).

E. Array Tip Speed

Fig. 7 shows the average tip speed for mediolateral angles of 0° and 40°, respectively, from 42 insertions with 11 dummies,

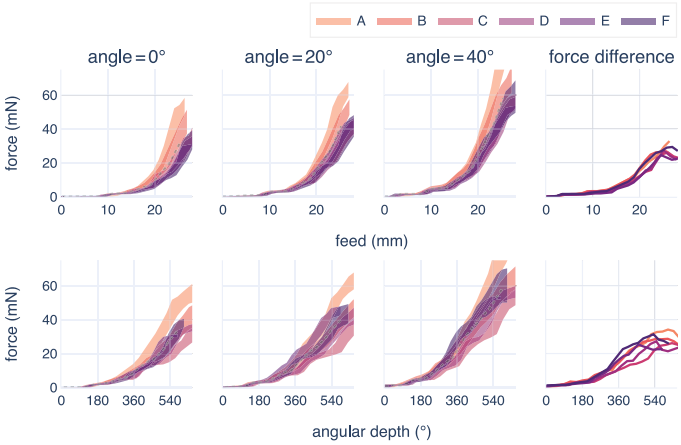

Fig. 6. Insertion forces for six different scala tympani models as a function of linear feed (top) and angular tip position (bottom). Insertions were performed at mediolateral angles of 0°, 20° and 40°, respectively, all at a basoapical angle of 0° and a speed of 0.33 mm/s. The data combines multiple experiments with 6-14 insertions per angle and model, using 3-7 dummies per model. Legend entries are sorted by cochlear size from small (model *A*) to large (model *F*). The shaded areas cover the first to third quartile of the recorded forces. The rightmost column shows the force differences between parallel and non-parallel insertions for each model.

Fig. 7. Tip speeds (first to third quartiles) from 42 insertions (11 dummies) into model *B* inserted at a parallel insertion axis (0° mediolateral and 0° basoapical) or a non-parallel insertion axis (40° mediolateral and 0° basoapical). The dashed horizontal line corresponds to the feed rate of the insertion (0.33 mm/s). The red and blue bar indicates regions with significant differences in tip speed between the parallel and non-parallel insertion ($p < 0.001$).

inserted at 0.33 mm/s and a basoapical angle of 0°. The congruency between the feed-forward speed, with which the array is pushed into the model and the speed of the array tip can be understood as a measure of the smoothness of the insertion. We observed significantly smoother movement of the array tip for parallel insertions. The upper part of the figure indicates statistically significant differences in tip speed and the t-statistic (independent two-sample t-test) of a moving window along the angular insertion depth. The increase in tip speed at around 135° is caused by the redirection of the array at first contact with the lateral wall. The subsequent drop in tip speed occurs as the array bends into the curvature of the lateral wall. This general behaviour was observed with all models and we found

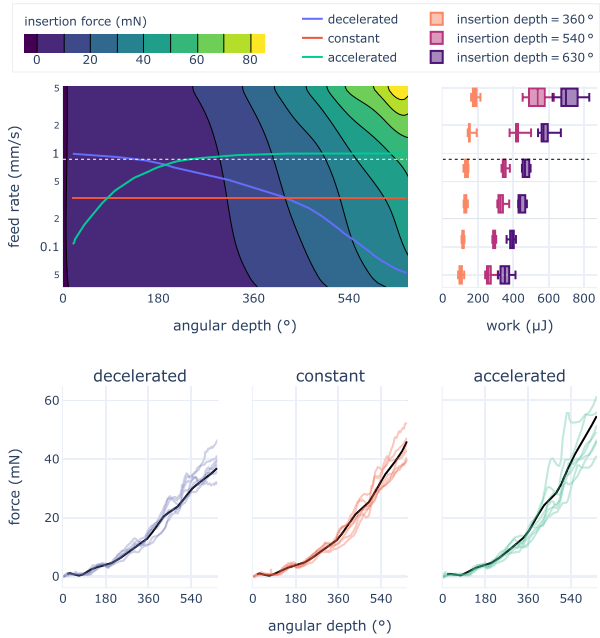

Fig. 8. Upper left: measured insertion forces versus angular insertion depth and insertion speed. The data shows 55 insertions with 5 dummies inserted at a moderate axis (20° mediolateral, 0° basoapical) into model *B*. Upper right: insertion energies of these insertions at 360°, 540°, and 630° angular insertion depth. The dashed line shows the lower bound for manual array insertion, according to [14]. Bottom row: predicted (black lines) and measured forces (colored lines) for decreasing, constant and increasing speeds, all with a total insertion duration of 78 s.The corresponding speed profiles are superimposed on the upper left graph.

no significant impact of the cochlear size on neither the minimum nor the maximum tip speeds.

At an intermediate insertion axis within the basal plane (20° mediolateral), we measured a smoothness of the tip speed in-between the two edge cases of a fully parallel insertion and a steep mediolateral angle of 40°, respectively.

F. Insertion Speed

Fig. 8 shows the forces (upper left) and insertion work (upper right) for insertion speeds between 0.05 mm/s and 4 mm/s (55 insertions of 5 dummies at 20° mediolateral and 0° basoapical). We observed a strong positive correlation between the insertion forces and the feed rate (Spearman's correlation coefficient $r = 0.94$, $p < 0.001$).

In contrast to the force differences arising from the alignment angle to the scala tympani (Section III-C), the forces here relax to a common value of 40 mN $\pm$ 3 mN. This steady state after the insertion is induced by the elastic deformation of the array and is independent of the preceding feed rate.

IV. Discussion

A. Contact Force

We observed that insertion forces increase substantially faster than predicted from the theoretical case of an array with negligible bending stiffness (c. f., (2)), with doubling angles of 116° and 331°, respectively. This indicates that the stiffness of the array

contributes significantly to the frictional forces, encouraging the trend towards more flexible modern arrays.

The friction model (Section II-E) estimates contact forces of 43 mN/mm in the basal region of the scala tympani and a tip contact force of 14 mN. Ishii *et al.* determined forces for penetrating the basilar membrane with a blunt needle (diameter 130 μm) of approximately 30 mN [16]. Schuster *et al.* measured forces to penetrate the interscalar partition (osseous spiral lamina, basilar membrane and Reissner's membrane treated as single entity) with a spherical indenter (diameter 300 μm) of 88 mN $\pm$ 25 mN [50]. The estimated normal forces are thus below the threshold at which a scalar translocation can be expected, but the difference is not very large. This is consistent with the low but non-zero rate of translocation found in implantation of modern lateral wall electrode arrays [51].

Previous temporal bone studies have found a majority of traumatic sites close to 180° [2], [19], [24], [52]. Torres *et al.* have suggested that some of these injuries are caused by the basal part of the array in later stages of the insertion [24]. Our findings support this hypothesis, as the distribution of normal forces along the array shows substantially larger forces in the basal region and during later stages of the insertion (c. f., Fig. 4).

B. Insertion Axis

We have observed no notable differences in the axis dependency between different models, and therefore limit the analysis of angular dependency to model *B*.

Several metrics indicate a positive impact of a parallel insertion axis. Insertion forces are significantly larger for non-parallel insertions (35 mN and 58 mN, for an angle in the basal plane of 0° and 40°, respectively, see Section III-C) and the mediolateral angle has a greater impact on the insertion forces than the basoapical angle.

However, we observed no difference in the array shape above 150° for different insertion axes. In addition, the force difference between parallel and non-parallel insertions as a function of linear feed of the array is independent of the model geometry and size (see Section III-D). Both findings indicate that the bulk of the additional forces associated with non-parallel insertions occur in the basal region of the scala tympani. Apically, the electrode arrays adopt a very similar trajectory due to their flexible nature.

In addition, we observed that the array tip moves significantly smoother when the array is inserted parallel to the scala tympani, especially through the first turn (c. f., Section III-E). A smoother array progression can be expected to be beneficial to the insertion progress, as it reduces local force peaks.

These considerations are consistent with increased rates of osseous spiral lamina fractures and more basally oriented translocations observed in non-parallel insertion angles by Torres *et al.* [24]. They may also partly explain the osseous spiral lamina fractures observed by Kaufmann *et al.* in manual insertions [19], where the alignment angle is less well controlled compared to the automated insertion.

Although our clinical data shows that parallel alignment angles are usually not accessible with round window insertions, optimal angles could potentially be achieved using specialized surgical tools or alternative surgical approaches. Even with respect to conventional cochlear implantation, our results suggest that the electrode array should be aligned with the goal of minimizing the mediolateral angle, in order to decrease insertion forces.

It should be noted that the anatomy of the round window region is very complex [53], [54], and the models used here have a widely opened entry point to ensure that the array only contacts intracochlear surfaces without perturbing the force measurements. In a surgical setting, the insertion axis does not necessarily correspond to the axis at which an electrode array approaches the cochlea, as its course may be altered by the geometry of the facial recess and the cochlear promontory.

C. Force Reduction With Non-Constant Insertion Speed

Several studies investigated the speed dependency of cochlear implantation with inconsistent results. A reduction in insertion forces for slow insertion speeds was found by Hügl *et al.* [15]. However, insertions were stopped at shallow depths of approximately 270°. Contrary to these findings, Zhang *et al.* measured smaller forces for fast insertions in a similar model [55]. Kaufmann *et al.* also observed increasing peak insertion forces for slower insertions into a synthetic model, but this was not reproduced in insertions into cadaveric cochleae [19].

In contrast to these previous studies, we used models with controlled frictional properties based on a hydrophilic polymer brush coating. We observed that slower insertion speeds effectively lead to lower insertion forces (c. f., Section III-F). These findings are consistent with measurements on cadaveric temporal bones [39]. Such a relation may not be evident at first, as frictional coefficients tend to depend little on sliding velocity and stick-slip events lead to increased friction at slow speeds [56], [57]. However, by advancing the electrode array, the elastic deformation induces stresses which can dissipate by frictional sliding. A slower feed rate provides more time for this process. In this case, the array is closer to the relaxed state, resulting in smaller forces.

This is reflected in the fact that the forces decay to a final value of 40 mN$\pm$3 mN after the insertion is stopped, independent of the insertion speed. In contrast, this final static force is not the same for different insertion angles (c. f., Section III-C) because the curvature of the array and therefore the elastic restoring force changes with the insertion angle.

An interesting consequence of this speed dependency is that peak forces can be reduced by slowing down the insertion towards the end. Different speed profiles with a total duration of 78 s (average feed rate of 0.33 mm/s) are shown in Fig. 8 (top left). The bottom row shows the measured forces for these decreasing, constant and increasing feed rates (colored lines) together with the prediction from constant speed measurements (black lines). Compared to a constant speed insertion, the peak insertion force can be significantly reduced with a decelerating feed-forward profile (39 mN $\pm$ 3 mN versus 44 mN $\pm$ 4mN). Conversely, an increasing insertion speed leads to higher peak forces (50 mN $\pm$ 6 mN).

Note that the feed-forward profiles used herein do not attempt to represent an optimal profile. Paths that minimize the maximal force or the insertion work can potentially be determined from the data of the speed dependency (see Fig. 8, top left). However, for clinical application, other factors such as the maximum speed and smoothness of motion may need to be considered as well.

D. Study Limitations

The use of artificial cochlear models enables repeated measurements with constant properties, which is not possible in ex-vivo insertions. The large number of insertion experiments would not have been possible in cadaver specimens for reasons of availability and specimen degradation. Thus we consider artificial models as a valid option for the initial verification of new CI electrode array insertion paradigms with the advantages of visualization and repeatability. In contrast to cadaveric samples, the artificial models can not simulate intracochlear trauma, as these structures are not present. Therefore, our results might not be directly transferable to clinical insertions. However, the specimen preservation influences the characteristics of biological tissue and therefore the comparability to in-vivo conditions also for cadaver studies. Formalin-fixed samples, for example, are less hydrated and have increased rigidity of intracochlear soft tissue. [32], [34].

We believe that the use of a hydrophilic coating and geometries directly obtained from image data of human specimens improves the applicability of our results to the in-vivo case. Future studies must be conducted to verify the properties of the models used and to ensure the validity of the current results.

Unlike previous studies [15], [35], [36], [55], [58], the orientation of our models is based on an assessment of the cochlear orientation in a real surgery. Due to anatomical variations and personal preferences of the surgeon, this orientation may vary to some degree, however the patients are bedded according to our standard clinical protocol in lateral position with the head in hyperextension, limiting this variation. Given that the influence of gravity is very small compared with the measured insertion forces, we do not expect that such variations in cochlear orientation would significantly affect our results.

Measurements of intracochlear pressure during the insertion revealed only small hydrostatic variations but no nontrivial findings. Therefore, they were not further detailed in the present analysis. This is not unexpected, as the motorized insertion results in steady movement of the dummy arrays, reducing pressure transients. Furthermore, the round window region is exposed to ensure that the array contacts only intracochlear surfaces and does not interfere with the force measurements. A more restrictive opening of the round window could potentially limit the outflow of intracochlear fluid that is displaced by the array and increase pressure, especially during fast insertions.

Another limitation of this study is that only one type of electrode array was tested. Other arrays, both straight and precurved, must be investigated to determine the influence of length, stiffness and construction type, enabling a comparison of their performance. Finally, the friction force model (Section II-E) is only applicable to free fitting lateral wall models and requires adaptation for perimodiolar arrays.

V. Conclusion

In this work, we used scala tympani models with accurate macro-anatomy and controlled frictional properties to analyze the impact of insertion speed and angle of approach on reaction forces, the smoothness of motion and the array curvature for deep insertions of lateral wall electrode arrays.

We found that insertion forces scale exponentially with the angular contact length of the electrode arrays, in accordance with a mathematical model of frictional forces. The contact forces increase substantially both in the later stages of the insertion and in the basal portion of the scala tympani.

As reported previously, parallel insertions result in lower forces throughout the insertion process. Our data suggest that these force differences are mainly induced in the basal region of the scala tympani, while the angle of approach plays a smaller role for forces occurring in the apical cochlear turn. Additionally, parallel insertions are associated with significantly smoother movement of the array tip, presumably reducing local stress peaks during insertions. In agreement with findings from previous cadaveric studies, we found that a slower feed rate decreases forces during the insertion process. Most importantly, we showed that non-constant feed-forward profiles with decreasing speed reduce the maximum occurring forces compared to a constant feed with the same total duration.

Our findings may contribute to provide optimized clinical guidelines, improved surgical tools for manual and robotic procedures [59] and refined electrode array designs to help reduce intracochlear trauma.

References

[1] J. T. Roland, "A model for cochlear implant electrode insertion and force evaluation: Results with a new electrode design and insertion technique," *Laryngoscope*, vol. 115, no. 8, pp. 1325–1339, Aug. 2005.

[2] Y. Nguyen *et al.*, "Cochlear implant insertion forces in microdissected human cochlea to evaluate a prototype array," *Audiol. Neurotol.*, vol. 17, no. 5, pp. 290–298, 2012.

[3] N. T. Jiam and C. J. Limb, "The impact of round window vs cochleostomy surgical approaches on interscalar excursions in the cochlea: Preliminary results from a flat-panel computed tomography study," *World J. Otorhinolaryngol. - Head Neck Surg.*, vol. 2, no. 3, pp. 142–147, Sep. 2016.

[4] W. Wimmer *et al.*, "Cone beam and micro-computed tomography validation of manual array insertion for minimally invasive cochlear implantation," *Audiol. Neurotol.*, vol. 19, no. 1, pp. 22–30, 2014.

[5] A. Dhanasingh and C. Jolly, "An overview of cochlear implant electrode array designs," *Hear. Res.*, vol. 356, pp. 93–103, Dec. 2017.

[6] C. Sierra *et al.*, "Preservation of residual hearing after cochlear implant surgery with deep insertion electrode arrays," *Otol. Neurotol.*, vol. 40, no. 4, pp. e373–e380, Apr. 2019.

[7] R. M. Huarte and J. T. Roland, "Toward hearing preservation in cochlear implant surgery," *Current Opinion Otolaryngol. Head Neck Surg.*, vol. 22, no. 5, pp. 349–352, Oct. 2014.

[8] E. Lehnhardt, "Intracochlear placement of cochlear implant electrodes in soft surgery technique," *HNO*, vol. 41, no. 7, pp. 356–359, 1993.

[9] C. James *et al.*, "Preservation of residual hearing with cochlear implantation: How and why," *Acta Oto-Laryngologica*, vol. 125, no. 5, pp. 481–491, May 2005.

[10] D. R. Friedland and C. Runge-Samuelson, "Soft cochlear implantation: Rationale for the surgical approach," *Trends Amplification*, vol. 13, no. 2, pp. 124–138, Jun. 2009.

[11] M. Mirsalehi *et al.*, "Insertion forces and intracochlear trauma in temporal bone specimens implanted with a straight atraumatic electrode array," *Eur. Arch. Oto-Rhino-Laryngol.*, vol. 274, no. 5, pp. 2131–2140, May 2017.

[12] G. P. Rajan, G. Kontorinis, and J. Kuthubutheen, "The effects of insertion speed on inner ear function during cochlear implantation: A comparison study," *Audiol. Neurotol.*, vol. 18, no. 1, pp. 17–22, 2013.

[13] L. B. Kratchman *et al.*, "Force perception thresholds in cochlear implantation surgery," *Audiol. Neurotol.*, vol. 21, no. 4, pp. 244–249, 2016.

[14] K. Kesler *et al.*, "Human kinematics of cochlear implant surgery: An investigation of insertion micro-motions and speed limitations," *Otolaryngol.-Head Neck Surg.*, vol. 157, no. 3, pp. 493–498, Sep. 2017.

[15] S. Hügl *et al.*, "Investigation of ultra-low insertion speeds in an inelastic artificial cochlear model using custom-made cochlear implant electrodes," *Eur. Arch. Oto-Rhino-Laryngol.*, vol. 275, no. 12, pp. 2947–2956, Dec. 2018.

[16] T. Ishii, M. Takayama, and Y. Takahashi, "Mechanical properties of human round window, basilar and reissner's membranes," *Acta Oto-Laryngologica*, vol. 115, no. sup519, pp. 78–82, Jan. 1995.

[17] J.-P. Kobler *et al.*, "An automated insertion tool for cochlear implants with integrated force sensing capability," *Int. J. Comput. Assist. Radiol. Surg.*, vol. 9, no. 3, pp. 481–494, May 2014.

[18] T. S. Rau *et al.*, "A simple tool to automate the insertion process in cochlear implant surgery," *Int. J. Comput. Assist. Radiol. Surg.*, vol. 15, no. 11, pp. 1931–1939, Aug. 2020.

[19] C. R. Kaufmann *et al.*, "Evaluation of insertion forces and cochlea trauma following robotics-assisted cochlear implant electrode array insertion," *Otol. Neurotol.*, vol. 41, no. 5, pp. 631–638, Feb. 2020.

[20] R. Torres *et al.*, "An optimized robot-based technique for cochlear implantation to reduce array insertion trauma," *Otolaryngol.–Head Neck Surg.*, vol. 159, no. 5, pp. 900–907, Nov. 2018.

[21] S. Vittoria *et al.*, "Robot-based assistance in middle ear surgery and cochlear implantation: First clinical report," *Eur. Arch. Oto-Rhino-Laryngol.*, vol. 278, pp. 77–85, May 2020.

[22] S. A. Wade *et al.*, "Measurement of forces at the tip of a cochlear implant during insertion," *IEEE Trans. Biomed. Eng.*, vol. 61, no. 4, pp. 1177–1186, Apr. 2014.

[23] A. N. Vadivelu *et al.*, "Integrated force sensor in a cochlear implant for hearing preservation surgery," in *Proc. 41st Annu. Int. Conf. IEEE Eng. Med. Biol. Soc.*. Berlin, Germany, 2019, pp. 3819–3822s.

[24] R. Torres *et al.*, "Cochlear implant insertion axis into the basal turn: A critical factor in electrode array translocation," *Otol. Neurotol.*, vol. 39, no. 2, pp. 168–176, Feb. 2018.

[25] D. De Seta *et al.*, "Damage to inner ear structure during cochlear implantation: Correlation between insertion force and radio-histological findings in temporal bone specimens," *Hear. Res.*, vol. 344, pp. 90–97, Feb. 2017.

[26] M. Drouillard *et al.*, "Influence of electrode array stiffness and diameter on hearing in cochlear implanted guinea pig," *PLOS ONE*, vol. 12, no. 8, Aug. 2017, Art. no. e0183674.

[27] T. Lenarz *et al.*, "First experience with a new thin lateral wall electrode in human temporal bones:," *Otol. Neurotol.*, vol. 40, no. 7, pp. 872–877, Apr. 2019.

[28] U. Kisser *et al.*, "Residual hearing outcomes after cochlear implant surgery using ultra-flexible 28-mm electrodes," *Otol. Neurotol.*, vol. 37, no. 7, pp. 878–881, Aug. 2016.

[29] P. S. Roland and C. G. Wright, "Surgical aspects of cochlear implantation: Mechanisms of insertional trauma," in *Adv. Oto-Rhino-Laryngol.*, vol. 64, pp. 11–30, 2006.

[30] P. Mukherjee *et al.*, "Assessment of intracochlear trauma caused by the insertion of a new straight research array," *Cochlear Implants Int.*, vol. 13, no. 3, pp. 156–162, Aug. 2012.

[31] J. Pile and N. Simaan, "Characterization of friction and speed effects and methods for detection of cochlear implant electrode tip fold-over," in *Proc. IEEE Int. Conf. Robot. Automat.* Karlsruhe, Germany, 2013, pp. 4409–4414.

[32] E. Avci *et al.*, "Three-dimensional force profile during cochlear implantation depends on individual geometry and insertion trauma," *Ear Hear.*, vol. 38, no. 3, pp. e168–e179, 2017.

[33] R. Torres *et al.*, "Improvement of the insertion axis for cochlear implantation with a robot-based system," *Eur. Arch. Oto-Rhino-Laryngol.*, vol. 274, no. 2, pp. 715–721, Feb. 2017.

[34] L. Anschuetz *et al.*, "Cochlear implant insertion depth prediction: A. temporal bone accuracy study," *Otol. Neurotol.*, vol. 39, no. 10, pp. e996–e1001, 2018.

[35] G. Kontorinis *et al.*, "Impact of the insertion speed of cochlear implant electrodes on the insertion forces:," *Otol. Neurotol.*, vol. 32, no. 4, pp. 565–570, Jun. 2011.

[36] L. Leon *et al.*, "Scala-tympani phantom with cochleostomy and round-window openings for cochlear-implant insertion experiments," *J. Med. Devices*, vol. 8, no. 4, Dec. 2014, Art. no. 041010.

[37] N. Gerber *et al.*, "A multiscale imaging and modelling dataset of the human inner ear," *Sci. Data*, vol. 4, Sep. 2017, Art. no. 170132.

[38] D. Sieber *et al.*, "The OpenEar library of 3D models of the human temporal bone based on computed tomography and micro-slicing," *Sci. Data*, vol. 6, Jan. 2019, Art. no. 180297.

[39] P. Aebischer, M. Caversaccio, and W. Wimmer, "Fabrication of human anatomy-based scala tympani models with a hydrophilic coating for cochlear implant insertion experiments," *Hear. Res.*, vol. 404, pp. 1–5 2021.

[40] C. Rathgeb *et al.*, "Clinical applicability of a preoperative angular insertion depth prediction method for cochlear implantation:," *Otol. Neurotol.*, vol. 40, no. 8, pp. 1011–1017, Sep. 2019.

[41] P. Aebischer *et al.*, "Intraoperative impedance-based estimation of cochlear implant electrode array insertion depth," *IEEE Trans. Biomed. Eng.*, vol. 68, no. 2, pp. 545–555, Feb. 2021.

[42] B. Escudé *et al.*, "The size of the cochlea and predictions of insertion depth angles for cochlear implant electrodes," *Audiol. Neurotol.*, vol. 11, no. 1, pp. 27–33, 2006.

[43] B. M. Verbist *et al.*, "Consensus panel on a cochlear coordinate system applicable in histologic, physiologic, and radiologic studies of the human cochlea," *Otol. Neurotol.*, vol. 31, no. 5, pp. 722–730, Jul. 2010.

[44] W. Wimmer, C. N. Vandersteen Guevara, M. Caversaccio, and H. Delingette, "Robust cochlear modiolar axis detection in CT," in *Medical Image Computing and Computer Assisted Intervention MICCAI 2019*, D. Shen, T. Liu, T. M. Peters, L. H. C. Staib Essert, S. Zhou, P.-T. Yap, and A. Khan, Eds. Cham, Switzerland: Springer, 2019, vol. 11768, pp. 3–10.

[45] W. Wimmer *et al.*, "Semiautomatic cochleostomy target and insertion trajectory planning for minimally invasive cochlear implantation," *BioMed Res. Int.*, vol. 2014, pp. 1–8, 2014.

[46] S. W. Attaway, "The mechanics of friction in rope rescue," in *Proc. Int. Tech. Rescue Symp.*, 1999, pp. 1–8.

[47] H. Kha and B. Chen, "Determination of frictional conditions between electrode array and endosteum lining for use in cochlear implant models," *J. Biomech.*, vol. 39, no. 9, pp. 1752–1756, Jan. 2006.

[48] J.-P. Kobler, A. Dhanasingh, R. Kiran, C. Jolly, and T. Ortmaier, "Cochlear dummy electrodes for insertion training and research purposes: Fabrication, mechanical characterization, and experimental validation," *BioMed Res. Int.*, vol. 2015, pp. 1–9, 2015.

[49] J. H. Jung, N. Pan, and T. J. Kang, "Generalized capstan problem: Bending rigidity, nonlinear friction, and extensibility effect," *Tribol. Int.*, vol. 41, no. 6, pp. 524–534, Jun. 2008.

[50] D. Schuster, L. B. Kratchman, and R. F. Labadie, "Characterization of intracochlear rupture forces in fresh human cadaveric cochleae," *Otol. Neurotol.*, vol. 36, no. 4, pp. 657–661, Apr. 2015.

[51] B. P. O'Connell, J. B. Hunter, and G. B. Wanna, "The importance of electrode location in cochlear implantation," *Laryngoscope Invest. Otolaryngol.*, vol. 1, no. 6, pp. 169–174, Dec. 2016.

[52] W. G. Morrel *et al.*, "Effect of scala tympani height on insertion depth of straight cochlear implant electrodes," *Otolaryngol.Head Neck Surg.*, vol. 162, no. 5, pp. 718–724, Feb. 2020.

[53] H. L. Cornwall, P. S. Marway, and M. Bance, "A micro-computed study of round window anatomy and implications for atraumatic cochlear implant insertion," *Otol. Neurotol.*, vol. 42, no. 2, pp. 327–334, Dec. 2020.

[54] M. Tóth *et al.*, "Development and surgical anatomy of the round window niche," *Ann. Anatomy - Anatomischer Anzeiger*, vol. 188, no. 2, pp. 93–101, Mar. 2006.

[55] J. Zhang, S. Bhattacharyya, and N. Simaan, "Model and parameter identification of friction during robotic insertion of cochlear-implant electrode arrays," in *Proc. IEEE Int. Conf. Robot. Automat.* Kobe, 2009, pp. 3859–3864.

[56] B. Lorenz *et al.*, "Static or breakloose friction for lubricated contacts: The role of surface roughness and dewetting," *J. Physics: Condens. Matter*, vol. 25, no. 44, Nov. 2013, Art. no. 445013.

[57] C.-F. Tu and T. Fort, "A study of fiber-capstan friction. 2. stickslip phenomena," *Tribol. Int.*, vol. 37, no. 9, pp. 711–719, 2004.

[58] M. Miroir *et al.*, "Friction force measurement during cochlear implant insertion: Application to a force-controlled insertion tool design," *Otol. Neurotol.*, vol. 33, no. 6, pp. 1092–1100, 2012.

[59] M. Caversaccio *et al.*, "Robotic middle ear access for cochlear implantation: First in man," *PLOS ONE*, vol. 14, no. 8, Aug. 2019, Art. no. e0220543.